Computers and Geotechnics 176 (2024) 106742

Contents lists available at ScienceDirect

Computers and Geotechnics

journal homepage: www.elsevier.com/locate/compgeo

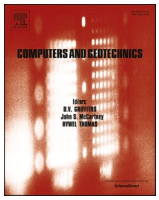

DEM evaluation of the mobilization of mechanisms governing the geogrid-aggregate interaction

Yafei Jia [a,b], Jorge G. Zornberg [b], Jun Zhang [c], Jun-Jie Zheng [a], Yewei Zheng [a,*]

[a] School of Civil Engineering, Wuhan University, Wuhan, Hubei 430072, China
[b] Maseeh Department of Civil, Architectural and Environmental Engineering, The University of Texas at Austin, Austin, TX 78712, USA
[c] Shanxi Transportation Technology Research & Development Co., Ltd., Key Laboratory of Highway Construction and Maintenance Technology in Loess Region, Taiyuan 030032, China

ARTICLE INFO

Keywords:
DEM
Geogrid
Aggregate
Pullout resistance
Interaction mechanism

ABSTRACT

Pullout tests of geogrids embedded in a single clean aggregate type were conducted and subsequently simulated to investigate the geogrid-aggregate interaction mechanisms. The Discrete Element Method (DEM) model, which was carefully calibrated and validated against the experimental results, was adopted for the simulations. The three-dimensional deformation behavior of geogrids and the shear behavior of aggregates with complex particle shapes were successfully predicted. Analysis of the particle displacement distribution and contact force distribution allowed determination of the particle-scale interaction mechanisms of the geogrid-aggregate system. In particular, the mobilization of pullout resistance components was tracked based on the contact identification method and the influence of geogrid stiffness on the mobilization of pullout resistance components could be evaluated. The results indicate that the activation of the different geogrid resistance components that develop during pullout are not synchronized. During the pullout process, DEM predictions indicate that the frictional resistance of the geogrid is activated first, peaking rapidly and being followed by the development of passive resistance of the transverse ribs. Also, an increased geogrid stiffness was found to enhance the passive resistance of the transverse ribs but to influence only negligibly the frictional resistance.

1. Introduction

The adoption of geogrids continues to increase worldwide as they are adopted in a continuously growing number of geotechnical systems, including their use to reinforce retaining walls, embankments, and foundations as well as to stiffen systems such as railway track beds, road bases, load transfer platforms and fill over voids (Bathurst and Naftchali, 2021; Indraratna et al., 2013; Jiang et al., 2016; Leshchinsky et al., 2010; Liu et al., 2007; Rowe and Li, 2005; Wang et al., 2022; Zornberg et al., 2000). In these applications, much of the benefits from the geogrid inclusions derive from their ability to interact with the surrounding soil particles through frictional and passive bearing mechanisms (Jewell et al., 1985). The complex interaction mechanisms between the geogrid and surrounding soils govern the performance of GRS structures. The optimal design of GRS structures requires a good understanding of the geogrid-soil interaction mechanism not only to predict the ultimate shear resistance but also to quantify the mobilization of different resistance components.

The characterization of the geogrid-soil interface is crucial for enhancing the understanding of the interactions between geogrids and soil. To this end, various testing methods have been developed, including pull-out tests, direct shear tests, in-soil tensile tests, and slope tests (Palmeira, 2009). Among these, pull-out tests and direct shear tests are extensively used to assess the conditions and applicability of geogrid-soil interactions. Several studies have quantified various resistance components in direct shear tests (Feng and Wang, 2023; Jia et al., 2024; Liu et al., 2009a; Liu et al., 2009b). However, pull-out tests may involve different mechanisms of resistance mobilization. While pull-out tests are primarily conducted to directly measure the pull-out resistance, they also provide valuable insights into the overall deformation behavior of the geogrid-aggregate composite. Previous studies (Abdi and Arjomand, 2011; Bergado and Chai, 1994; Ferreira et al., 2015; Mahigir et al., 2021; Moraci and Recalcati, 2006; Morsy et al., 2019b; Roodi and Zornberg, 2017; Sugimoto et al., 2001) have provided extensive

* Corresponding author.
E-mail addresses: yafeijia@whu.edu.cn (Y. Jia), zornberg@mail.utexas.edu (J.G. Zornberg), zj_sxjt@hotmail.com (J. Zhang), zhengjunjie@whu.edu.cn (J.-J. Zheng), yzheng@whu.edu.cn (Y. Zheng).

https://doi.org/10.1016/j.compgeo.2024.106742
Received 4 July 2024; Received in revised form 22 August 2024; Accepted 5 September 2024
Available online 12 September 2024

experimental results to evaluate the influence on the pullout resistance of parameters such as geogrid geometry, geogrid stiffness, aggregate size and gradation, backfill density, and stress level. However, physical tests provide limited insight into the micro-scale response at the geogrid-soil interface as well as little ability to visualize the progression of failure patterns. Although recent advances in high-precision imaging, transparent soils, and microscopic image analysis techniques offer qualitative insight, accurate and quantitative tracking of the mobilization of resistance components at the geogrid-soil interface has remained challenging (Bathurst and Ezzein, 2015, 2017; Derksen et al., 2021; Ezzein and Bathurst, 2014; Peng and Zornberg, 2019; Zhou et al., 2012). In particular, experimental difficulties have been reported regarding the techniques to accurately capture and interpret the interaction between the geogrid and surrounding soil during pullout tests.

In this regard, numerical modeling is an effective complement to laboratory testing to understand the fundamental behavior to geogrid-soil interaction under pullout conditions. Several studies have employed continuum methods, such as the Finite Element Method (FEM), to simulate geogrid-soil interaction (Abdi and Mirzaeifar, 2017; Hussein and Meguid, 2016, 2020; Sugimoto and Alagiyawanna, 2003). However, Palmeira (2004) indicates that conventional FEM simulations, which generally treat geogrid elements as equivalent planar friction layers with identical pullout resistance, cannot reproduce the actual geogrid-soil interaction mechanism. In certain applications, this method may lead to inaccurate strain predictions in the geogrid and surrounding soil. This is because of the limited ability of FEM simulations to account for the shape of aggregate particles and geogrids as well as for their complex interactions.

The Discrete Element Method (DEM) has emerged as a powerful tool to realistically model soil-geosynthetic interaction (Gu et al., 2017; Han et al., 2012; Wang et al., 2014). This method can simulate the actual irregular surface morphology of aggregate and evolving contact forces that develop among individual particles. In addition, DEM also facilitates achieving adequate representation of geogrid geometry, aperture size, stiffness, and interface characteristics. Previous studies have been conducted using DEM to investigate geogrid-aggregate interaction from idealized spherical particles or assemblies of aggregated spheres (Feng and Wang, 2023; Miao et al., 2017; Miao et al., 2020; Ngo et al., 2014; Stahl et al., 2014). Geogrids have been modeled using bond contact logic between particles (Chen et al., 2018; Jia et al., 2023; Stahl et al., 2014). These DEM simulations provide useful insight into the evolution of contact force chains and interfacial strains in geogrids during pullout testing. However, they have generally adopted simplified models to represent geogrid geometries and aggregate shapes, which may have compromised the accuracy of the predictions (Ferellec and McDowell, 2010; Tutumluer et al., 2012). A more realistic representation of actual particle morphology and geogrid geometry would be beneficial to better capture the deformation response and mobilization of different interaction mechanisms during pullout. The focus of recent studies on geogrid-aggregate interaction has shifted to comparatively more sophisticated DEM modeling using clusters of bonded spheres to simulate irregular particle shapes and geogrids using assembled spheres that are connected by parallel bonds (Chen et al., 2018; Ferellec and McDowell, 2012; Wang et al., 2024; Wang and Feng, 2023). The implementation of these advanced modeling techniques allows for a more detailed examination of contact force distributions and mobilized strains in geogrids during shearing. However, most research has calibrated these geogrid models based on planar tensile behavior, neglecting the three-dimensional (3D) deformation characteristics. And advanced 3D DEM modeling may provide an opportunity to gain deeper insights into geogrid pull-out behavior, taking into account the complex three-dimensional interactions and deformations that occur in practical applications.

This study involves a 3D DEM investigation into the pullout response of geogrids embedded in a clean aggregate, with a particular focus on revealing the mobilization of the different pullout resistance components. The impact of aggregate shape and 3D deformation of geogrid are fully evaluated in the simulations. The mobilization of pullout resistance components is tracked based on the contact force distributions, interfacial slip, and strain localization patterns at the particle scale. Overall, this study aims to provide an improved understanding of the load transfer mechanism of the geogrid-aggregate interface.

2. DEM modeling and parameter calibration

DEM modeling was conducted using the software Particle Flow Code 3D to simulate the pullout behavior of geogrid-aggregate interfaces. This section describes the DEM modeling procedures adopted in this study for the geogrid, aggregate particles, and pullout tests. The micromechanical parameters were calibrated based on experimental results to capture the physical characteristics of materials and interface behavior.

2.1. Geogrid

A biaxial polypropylene geogrid was used in this study. The longitudinal and transverse ribs of a biaxial geogrid correspond to the ribs in the machine direction (MD) and cross-machine direction (CMD), respectively. The geometric parameters of the geogrid ribs are listed in Table 1. The geogrid was simulated using bonded spherical particles with different sizes arranged in a grid pattern to reflect the actual aperture geometry, as shown in Fig. 1. Specifically, the geogrid was modeled using particle strings with diameters ranging from 1.5 mm to 3 mm between the joints to capture the variation in section thickness.

The linear parallel bond model (Potyondy and Cundall, 2004) was used to simulate the contacts between the particles of the geogrid model. This contact model, which allows for transfer of the axial forces along the ribs as well as bending and torsional moments between the bonded particles, has been previously utilized to simulate the tensile behavior of geogrids (Chen et al., 2018; Feng and Wang, 2023; Ferellec and McDowell, 2012; Jia et al., 2023). The parallel bond behaves like a cementitious material deposited between spheres with defined normal and shear stiffness values. The total force and moment increments in each parallel bond over a timestep can be calculated as:

$$\Delta\overline{F}_n = \overline{k}_n\overline{A}\Delta U_n \tag{1}$$

$$\Delta\overline{F}_s = \overline{k}_s\overline{A}\Delta U_s \tag{2}$$

$$\Delta\overline{M}_b = \overline{k}_n I\Delta\theta_b \tag{3}$$

$$\Delta\overline{M}_t = \overline{k}_s J\Delta\theta_t \tag{4}$$

where $\Delta\overline{F}_n$ and $\Delta\overline{F}_s$ are the normal and shear force increments, respectively; $\Delta\overline{M}_b$ and $\Delta\overline{M}_t$ are the bending and twisting moment increments, respectively; $\overline{k}_n$ and $\overline{k}_s$ are the normal and shear stiffness, respectively; ΔU_n and ΔU_s are the normal and shear relative displacement increments (tension), respectively; $\Delta\theta_b$ and $\Delta\theta_t$ are the relative rotation increments in bending and twisting, respectively; and I and J are the moment of inertia and polar moment of the bond cross-section, respectively.

Single rib tensile tests along the MD and CMD were conducted according to ASTM D6637 (ASTM, 2015). It is important to note that the

Table 1
Geogrid geometric parameters.

Geogrid ribs	Aperture size (mm)	Junction thickness (mm)	Junction width (mm)	Minimum rib thickness (mm)	Minimum rib width (mm)
MD	65	6	10	3	5
CMD	65	5	9	3	4

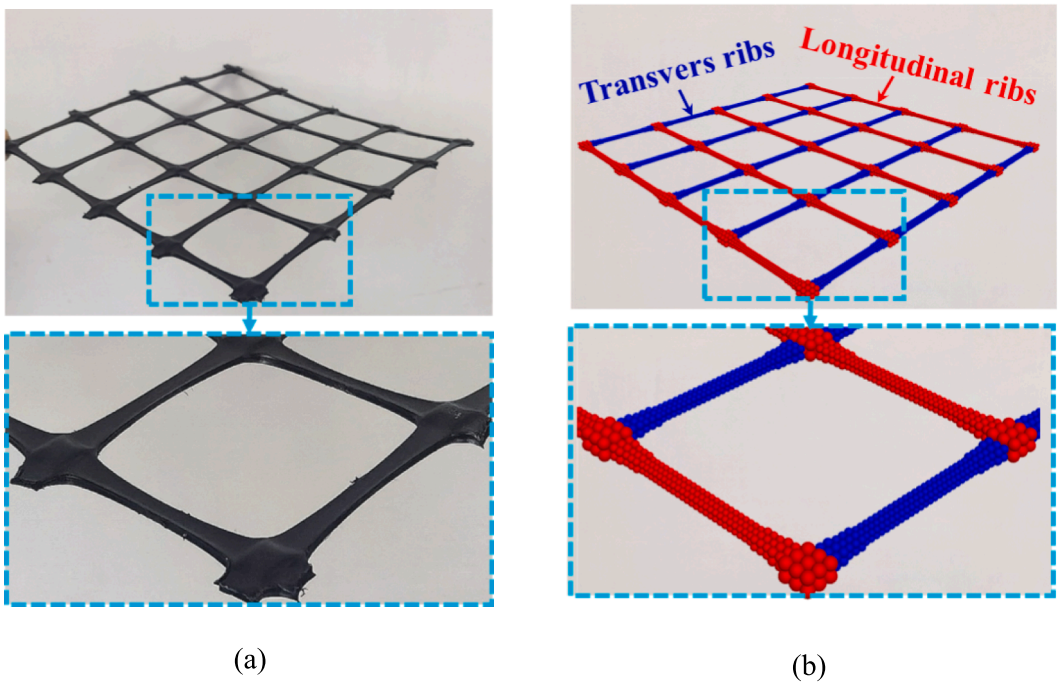

Fig. 1. Biaxial geogrid used in this study: (a) actual geogrid; and (b) geogrid model.

tensile behavior of polypropylene geogrids exhibits rate-dependency, as demonstrated by Shinoda and Bathurst (2004) and Bathurst and Naftchali (2021). In this study, the tensile tests were conducted at a strain rate of 10 %/min in accordance with the ASTM D6637 (ASTM, 2015) recommendation. This strain rate was selected to represent typical construction strain rates and enable direct comparisons with other studies on similar biaxial polypropylene geogrid products. The tensile response of the geogrid was calibrated by simulating tensile tests and comparing the predicted and experiment results, as shown in Fig. 2. The experimental data show a tensile behavior of the geogrid ribs characterized by an initial linear response followed by a nonlinear increase in tensile force with increasing tensile strains. The tensile behavior of the geogrid in DEM simulations is governed by the bond effective modulus, $\overline{E}_g^*$. The nonlinear tensile behavior can be described

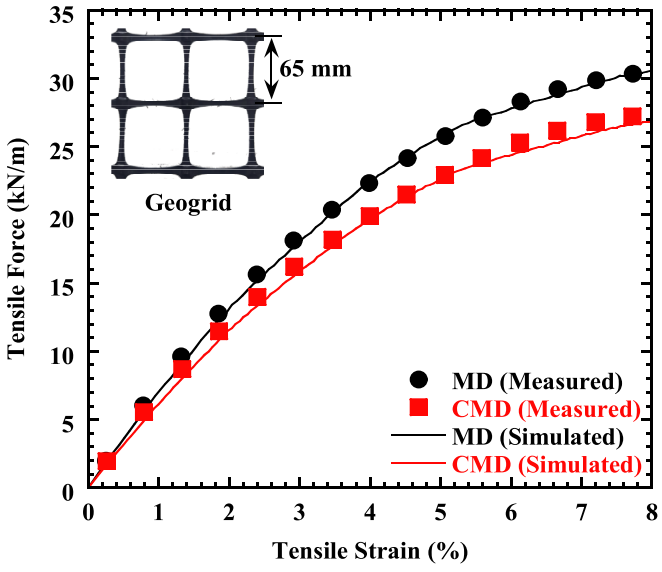

Fig. 2. Comparison between experimental results and DEM simulation predictions from single rib tensile tests.

using segmented linear functions of bond effective modulus and local tensile strain ε_l of the linear parallel bond contacts (Wang et al., 2014). In this study, the nonlinear tensile behavior of geogrid ribs is represented by three stages that depend on the local tensile strain, as follows:

$$\overline{E}_g^* = \overline{k}_n L = \begin{cases} \lambda_1 \overline{E}_{ini} & (0 < \varepsilon_l \le 2\%) \\ \lambda_2 \overline{E}_{ini} & (2\% < \varepsilon_l \le 5\%) \\ \lambda_3 \overline{E}_{ini} & (5\% < \varepsilon_l) \end{cases} \tag{5}$$

$$\varepsilon_l = \frac{D - L}{L} \times 100\% \tag{6}$$

where λ is a softening coefficient; E_{ini} is the initial bond effective modulus (tension only) of the geogrid ribs; D is the center distance between two particles in contact; and $L = R_1 + R_2$ is the contact length, which can be represented as the sum of the radius of two pieces in contact. The softening coefficients for the three stages are as follows: $\lambda_1 = 1.0$ for the first stage ($0 < \varepsilon_l \le 2\%$), $\lambda_2 = 0.7$ for the second stage ($2\% < \varepsilon_l \le 5\%$), and $\lambda_3 = 0.2$ for the third stage ($5\% < \varepsilon_l$). As indicated in Fig. 2, the simulation predictions agree well with the experimental results. For instance, the geogrid secant stiffness values at 2 % strain along the MD obtained from experiments and simulations were 680 kN/m and 650 kN/m, respectively.

After defining the axial tensile characteristics, additional calibration was performed to capture the out-of-plane bending and torsional behavior of the biaxial geogrid. Two-aperture extension tests were simulated by supporting a section of the geogrid specimen on two opposite transverse ribs and applying a transverse displacement. The relative normal and shear stiffness values between the parallel bonds were calibrated by comparing the predicted deformations to the experimental results. As shown in Fig. 3, the geogrid exhibited localized deformation, with the middle transverse rib buckling upward while the longitudinal ribs rotated outward. At a tensile force $F_t = 0.28$ kN, the upward buckling of the middle transverse rib of the geogrid does not continue to grow. The ratio between the maximum vertical displacement (out-of-plane, along the z-axis) of the transverse ribs to the distances between the two intermediate joints, h_f/d, obtained from simulations and tests at this tensile force are 0.28 and 0.30, respectively. The final calibrated geogrid parameters, which allowed the DEM model

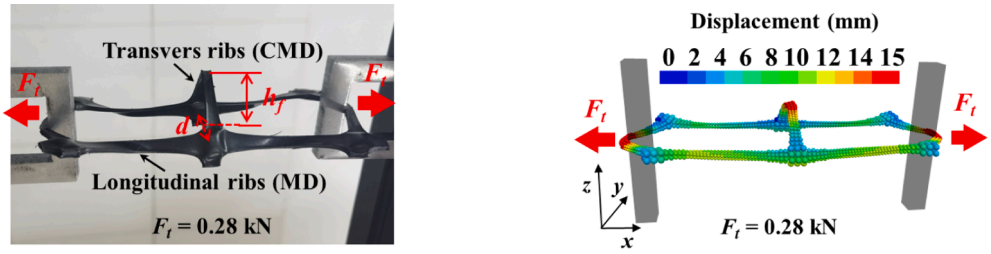

Fig. 3. Comparison of experimental results and DEM predictions from two-aperture extension tests: (a) experiment; and (b) DEM simulation.

to reproduce the tensile response of the biaxial geogrid in a realistic manner for in-plane and out-of-plane directions, are provided in Table 2.

2.2. Aggregates

The aggregates used in the experiments consisted of clean angular gravel-size particles. Previous studies have demonstrated that particle shape has a notable effect on the shear behavior of aggregates (Ferellec and McDowell, 2010; Gao and Meguid, 2018; Grabowski et al., 2021). Angular particles typically increase shear strength due to enhanced interlocking, whereas more rounded particles usually have lower shear strength of geogrid-aggregate interface (Liu et al., 2021; Miao et al., 2017). In the DEM simulation, irregularly shaped particles were created by filling the volume of closed 3D polyhedrons, representing the actual particles, with 'clump' logic. Specifically, the volume of real particles is filled with overlapping spheres to form "clumps." A point cloud representing the surface of the real particles was initially obtained through 3D scanning, after which the spheres were randomly launched at surface points and maximized within the particle volume along the surface normal. The larger the number of spheres, the higher the resolution of the particle shape. In addition, the spheres were given equal mass rather than equal density to improve the mass distribution within each clump. Irregular shapes have been demonstrated to provide better interlocking between particles and geogrids than simple spheres (Ferellec and McDowell, 2012). The volume error of the simulated particles relative to the real particles was used to evaluate the particle shape error in the numerical simulations. The volume error, E_V, can be expressed as follows:

$$E_V = \frac{|V_p - V_m|}{V_p} \tag{7}$$

where V_p is the volume of the prototype particle, and V_m represents the volume of the modeled particle in simulations. Fig. 4(a) presents the simulated particles with different volume errors (E_{V1} = 0.021, E_{V2} = 0.046, E_{V3} = 0.087 and E_{V4} = 0.125). The particle size distribution in the simulation is consistent with that of the aggregate used in the experiments, as shown in Fig. 4(b). The shear strength envelopes corresponding to particles with different volume errors are compared in Fig. 5 against experimental results determined by direct shear tests. Both the upper and lower shear boxes have a height of 200 mm and a width of 300 mm. The length of the upper shear box along the shear direction is 300 mm, while the length of the lower shear box is 360 mm. The larger area of the lower shear box ensures a constant contact area during the shearing process. Further details regarding the direct shear tests and numerical simulations are reported by Jia et al. (2024). To reach a balance between computational efficiency and accuracy, particles with E_{V3} = 0.087 were ultimately selected for the simulations conducted in this study.

Table 2
Geogrid model parameters.

Parameter	Value
Density, ρ_g (kg/m^3)	972
Local damping coefficient, d_p	0.7
Frictional coefficient, μ_g	0.44
Effective modulus, E_g^* (MPa)	3.52×10^4
Normal-to-shear stiffness ratio, κ_g^*	1
Longitudinal rib bond effective modulus, $\bar{E}_{ini}$ (MPa)	4×10^4
Transverse rib bond effective modulus, $\bar{E}_{ini}$ (MPa)	3.52×10^4
Bond normal-to-shear stiffness ratio, $\bar{\kappa}_g^*$	1×10^2
Bond radius multiplier, $\bar{r}_m$	1
Bond gap, $\bar{g}$ (m)	0.75×10^{-3}

The interaction between aggregate particles was simulated using a linear contact model (Cundall and Strack, 1979) characterized by normal and shear stiffness springs and a friction slider, as follows:

$$\Delta F_n = k_n \Delta U_n \tag{8}$$

$$\Delta F_s = k_s \Delta U_s \tag{9}$$

$$F_s \le \mu_a F_n \tag{10}$$

where ΔU_n and ΔU_s are the incremental normal and shear displacements (compression), respectively; k_n and k_s are the normal and shear stiffness values, respectively; and μ_a is the interparticle frictional coefficient. The normal and shear stiffness can be determined by assigning the effective modulus E_a^* and the normal-to-shear stiffness ratio κ_a^* to aggregate-aggregate contacts, as follows:

$$k_n = \frac{AE_a^*}{L} \tag{11}$$

$$\kappa_a^* = \frac{k_n}{k_s} \tag{12}$$

where A is the contact area; and L is the contact length. The micro-mechanical parameters were calibrated by matching the shear strength response from experimental data under normal stresses (σ_n) of 12.5 kPa, 25 kPa, and 50 kPa. As shown in Fig. 6, the shear strength responses predicted by DEM simulations agree well with the experimental results. The calibrated parameters adopted for the DEM simulations are provided in Table 3.

2.3. Pullout tests

The experimental pullout test apparatus used in this study (Fig. 7) consists of a rigid steel box with interior dimensions of 300 mm × 300 mm × 400 mm (length × width × height). The front wall of the box has a 10 mm-high opening that allows clamping and pullout of the geogrid specimen. To prevent obstruction of the opening by aggregate particles during pullout, the transverse ribs near the box edge were trimmed following the recommendation reported by Stahl et al. (2014). A normal (vertical) load was applied on top of the steel box using an actuator that connecting to a loading plate on an air bag to maintain a constant normal stress (σ_n). The geogrid specimen was fixed to a clamp connected

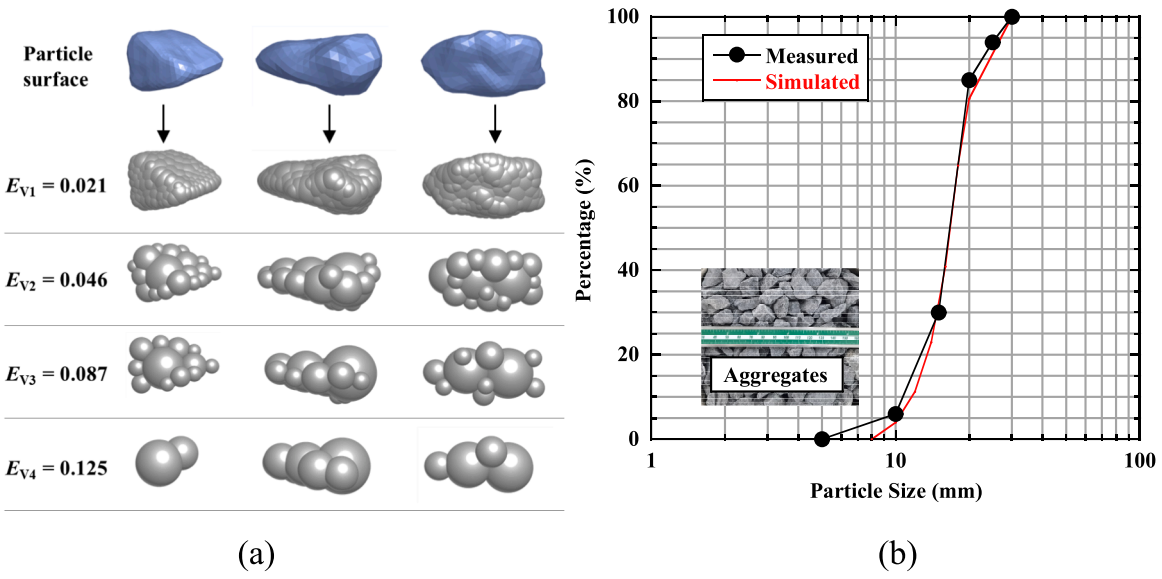

Fig. 4. Particles in DEM simulations: (a) individual particle shapes; and (b) particle size distribution.

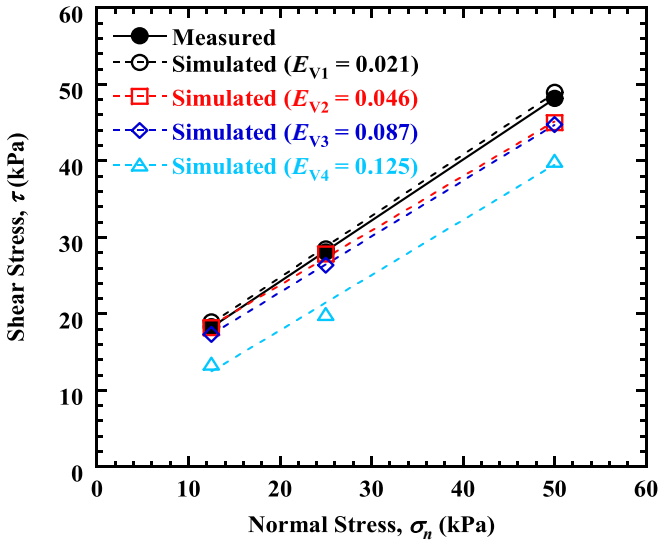

Fig. 5. Shear strength envelopes of particles with different volume errors.

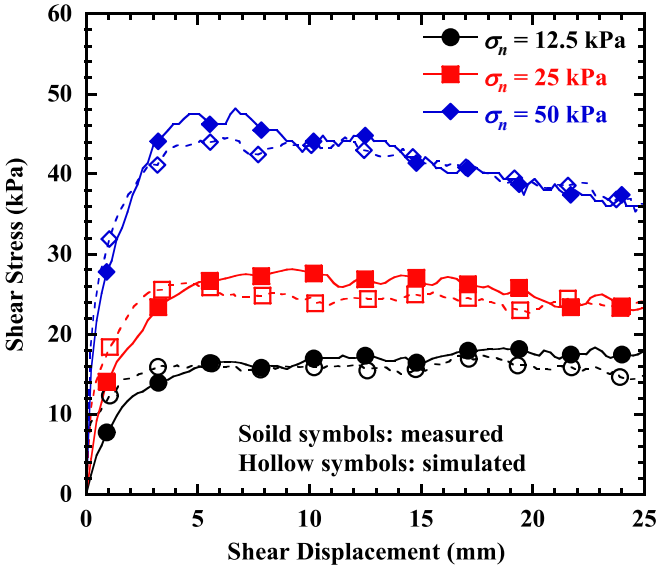

Fig. 6. Comparison of experimental results and DEM predictions from direct shear tests.

to a horizontal actuator that applied pullout force at a constant displacement rate while the rear end of the specimen was not clamped. The longitudinal and transverse ribs were oriented parallel and perpendicular to the pullout direction, respectively. A target soil density of $\rho_c = 1600.5$ kg/m^3 was selected during the preparation of the soil specimen. A constant pullout rate $v_p = 1$ mm/min was applied to the actuator until reaching a pullout displacement of 48 mm. The pullout tests were conducted under three different normal stresses of $\sigma_n = 12.5$ kPa, 25 kPa, and 50 kPa.

The DEM model adopted in this study (Fig. 8) incorporated the key features of the experimental setup. Specifically, the pullout box boundaries were modeled as rigid walls, and mirrored the dimensions in the experimental setups. It is important to note that the use of a rigid top boundary in the simulation might overestimate the pullout force compared to a flexible top boundary, which better accommodates soil deformations (Palmeira and Milligan, 1989). For instance, Wang et al. (2023) have shown in their DEM simulations that models with rigid top boundaries produced higher pullout forces than those with flexible top boundaries, with this trend becoming more pronounced under higher normal stresses. However, under lower normal stress levels (below 50 kPa), the difference between the two boundary conditions was minimal, with discrepancies within 1–2 kN/m. Aggregate particles were generated inside the box to match the target initial density of the specimens using a gravitational field of 9.8 m/s^2. A portion of the geogrid was installed beyond the front box wall and the longitudinal ribs were oriented parallel to the pullout direction to reflect the test configuration.

Table 3
Aggregate particle model parameters.

Parameter	Value
Density, ρ_a (kg/m^3)	2650
Local damping coefficient, d_p	0.7
Frictional coefficient, μ_a	0.55
Effective modulus, E_a^* (MPa)	2×10^3
Normal-to-shear stiffness ratio, κ_a^*	1

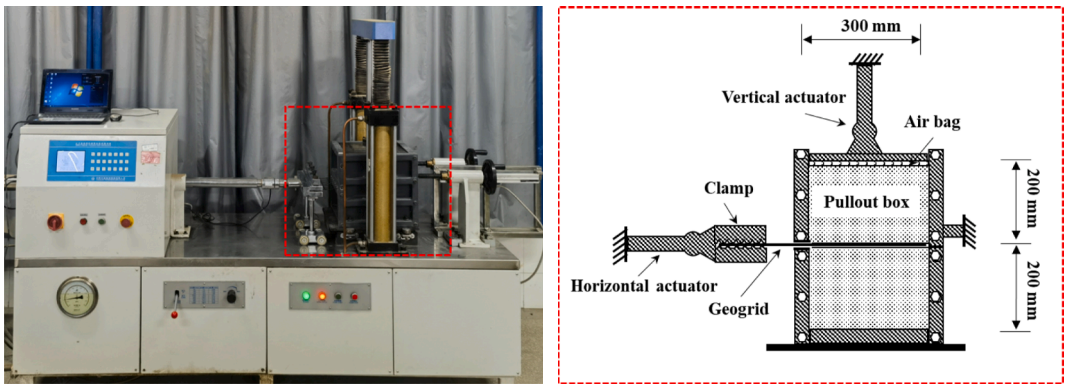

Fig. 7. Pullout apparatus used in this investigation: (a) view of the test setup; and (b) detail of the pullout box.

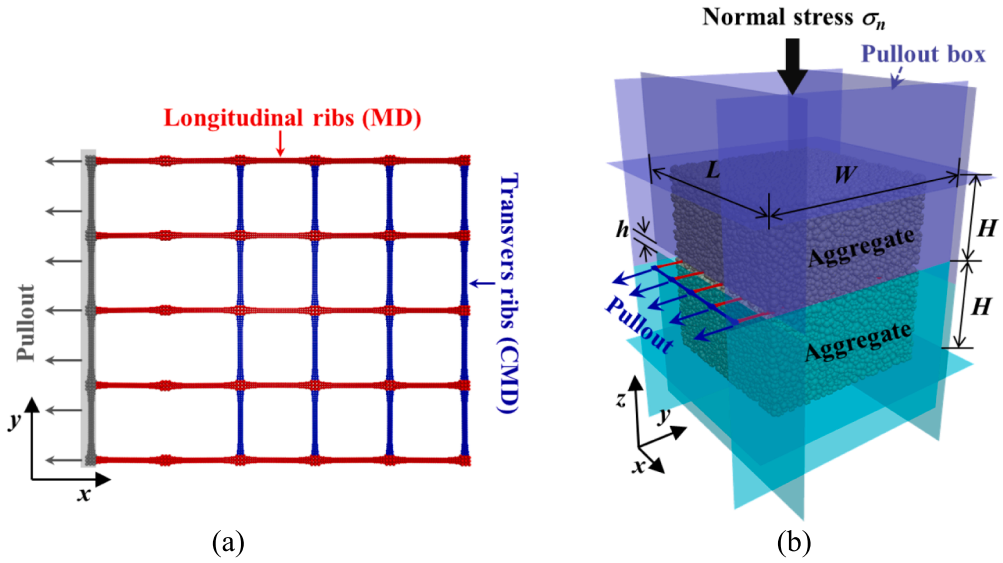

Fig. 8. DEM model of pullout test of geogrid specimens: (a) geogrid model; and (b) model of the pullout test setup.

Pullout tests were simulated by applying an increasing pullout load under a constant displacement rate to the clamped section of the geogrid.

The linear contact model (Cundall and Strack, 1979) was also employed to simulate the interaction between the geogrid and aggregate particles. Fig. 9 shows a comparison between the pullout experimental test results and the DEM predictions. Overall, the DEM predictions were found to agree well with the experimental results. The comparison indicates that the DEM model developed in this study accurately captured the development of pullout force with increasing displacement, including the initial nonlinear response and the behavior after achieving the pullout resistance of the geogrid. The parameters of the interface between geogrid and aggregates adopted in the DEM simulations are listed in Table 4. It should be noted that the interface parameters listed in Table 4 are those between the polymeric ribs and the aggregates. The parameters in Table 3, on the other hand, still apply to the contacts within the geogrid openings (aggregate-aggregate contacts).

3. DEM simulation results

This section presents an analysis of the DEM simulation results corresponding to the pullout test conducted under a normal stress of 12.5 kPa. This simulation is suitable to illustrate the different analyses conducted in this study, including the determination of shear bands, contact force distribution, and geogrid deformation in pullout tests. These results provide the basis for the subsequent approach to quantify the mobilization of different pullout resistance components based on contact identification.

3.1. Particle displacements and shear band thickness

The approach adopted in this study to quantify and visualize the intricate zones of particle-scale localized strain in granular soils, based on the relative displacement (*RD*) of particles, is consistent with that proposed by Druckrey and Alshibli (2017). The concept of relative particle displacement stems from kinematic displacements and is related to the displacement vector of a particle (δ) relative to that of all particles in contact with it (δ_i), using the second-order norm of vector differences:

$$rd_i = norm(\delta - \delta_i) \tag{13}$$

$$RD = \frac{1}{n}\sum_{i=1}^{n} rd_i \tag{14}$$

where rd_i is the relative displacement magnitude for a single contacting neighboring particle and n is the number of contacting particles. The

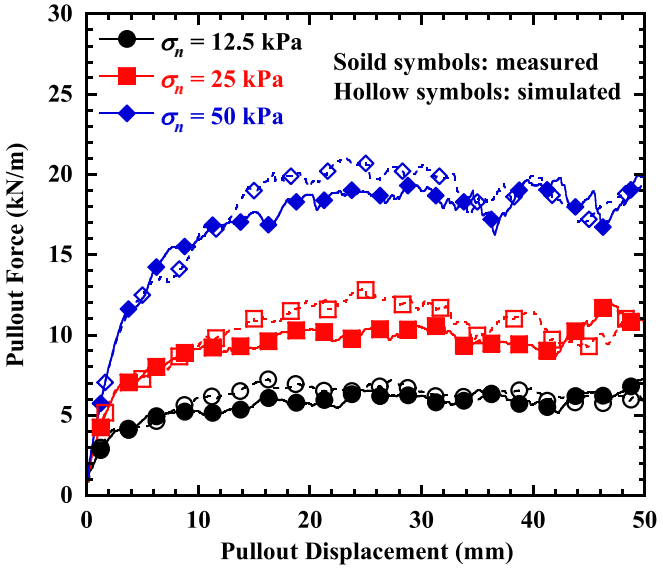

Fig. 9. Comparison between experimental results and DEM predictions for the geogrids during pullout testing.

Table 4
Parameters of the geogrid-aggregate interface.

Parameter	Value
Frictional coefficient, μ_{g-a}	0.44
Effective modulus, E^*_{g-a} (MPa)	1.5×10^3
Normal-to-shear stiffness ratio, κ^*_{g-a}	1

overall relative displacement magnitude is the average of all individual relative displacement vectors. Quantification of *RD* involves not only the displacements in the testing direction (i.e., horizontal), but also the displacements in any 3D direction. Therefore, *RD* can be used to capture the local shear behavior at the particle scale to clearly visualize the process of shear band formation. The distribution of the *RD* values of the particles for increasing pullout displacements δ_p are shown in Fig. 10, where the *RD* values have been normalized in relation to the maximum *RD* value for each pullout displacement. The *RD* distributions indicate that the shear bands (represented by higher *RD* values) start at the location of the geogrid and thickened as pullout displacement increased. At the end of the test (i.e., $\delta_p = 48$ mm), the thickness of the shear band is reasonably uniform along the entire length of the geogrid.

The gradient of the particle displacements along the pullout direction may be useful to quantify the thickness of the shear band (Jing et al., 2018). The shear strains during pullout occur in a narrow zone near the geogrid. Accordingly, the horizontal displacement of particles along the pullout direction (x-axis in the negative direction) and elevation in the normal (vertical) direction (z-axis) was used to quantify the thickness of shear bands (DeJong and Westgate, 2009). The average horizontal displacement (δ_x) was calculated by averaging the horizontal displacement component of particles along the pullout direction of the particles at the same elevation. Fig. 11 shows the distribution of the horizontal displacements of the particles and their averages at the same elevation versus the vertical distance from the geogrid location (d_v). Additional calculations were performed to define a smooth δ_x-d_v curve $f(d_v)$ using spline interpolation. Next, the first-order derivative $f'(d_v)$ and second-order derivative $f''(d_v)$ were obtained utilizing the finite difference method. The curvature κ was calculated as follows:

$$\kappa = \frac{|f''(d_v)|}{(1+f'(d_v)^2)^{3/2}} \tag{15}$$

As recommended by Jing et al. (2018), a curvature $\kappa = 0.02$ mm^{-1} was adopted to define the boundaries of the shear band. As shown in Fig. 11, for a pullout displacement $\delta_p = 48$ mm, the largest particle displacements occur at the elevation of the geogrid location, and the

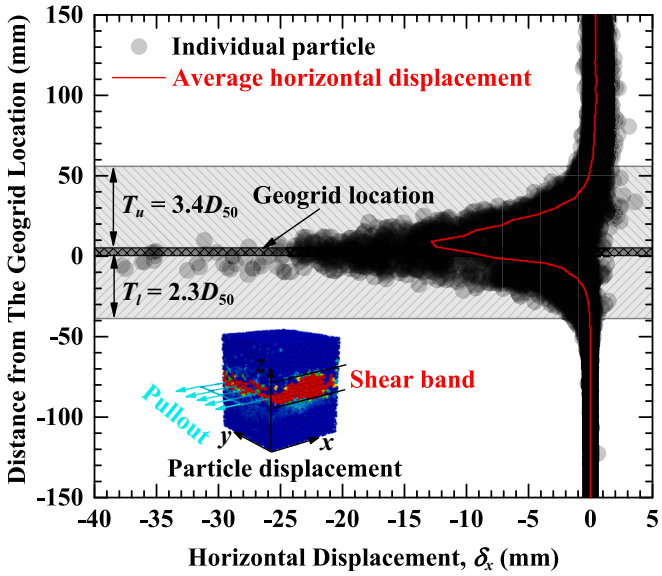

Fig. 11. Visualization of the shear band through evaluation of average horizontal displacements at the end of pullout testing.

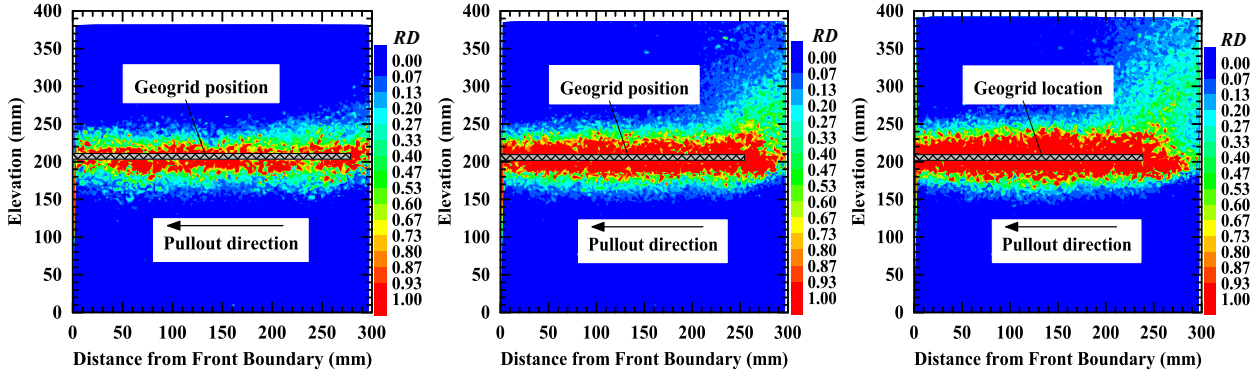

Fig. 10. Normalized relative displacement distribution at increasing pullout displacements: (a) $\delta_p = 6$ mm; (b) $\delta_p = 24$ mm; and (c) $\delta_p = 48$ mm.

horizontal particle displacements are observed to decrease with increasing distance from such elevation. The actual pattern is expected to depend on the friction between the particles and geogrid as well as the interlocking of particles located within the geogrid apertures. This results in the shear bands above and below the geogrid were found not to follow identical patterns. The upper shear band was found to be slightly larger than the lower one. Specifically, and considering an average particle size $D_{50} = 16.8$ mm, the upper shear band can be characterized by a thickness of 57.1 mm, which corresponds to $T_u = 3.4D_{50}$ while the lower shear band shows a thickness of 38.6 mm, corresponding to $T_l = 2.3D_{50}$. To maintain a constant normal stress, upward particle movement is possible if the geogrid-aggregate interface tends to dilate under shear, which ultimately results in a slightly thicker shear band developing above the geogrid than that developing below it. It is worthy that previous studies on the interaction between sand and various geosynthetics report shear band thicknesses ranging from $3.8D_{50}$ to $10D_{50}$ (DeJong and Westgate, 2009; Lashkari and Jamali, 2021). Vangla and Latha (2015) reported that shear band thickness tends to increase with larger particle sizes, while the normalized thickness (T/D_{50}) decreases. In this study, the shear band thickness at the geogrid-aggregate interface for larger aggregates ranges from $2.3D_{50}$ to $3.4D_{50}$, which is consistent with these findings (Vangla and Latha, 2015).

3.2. Contact force distributions

Fig. 12(a) presents the projection of the contact force chains within the specimen in the *x-o-z* plane at a pullout displacement of 48 mm, where the thickness of the lines represent the relative magnitude of the contact forces. The contact forces within the geogrid reinforcement are predominantly in tension (shown as red chains), while the aggregate-aggregate and geogrid-aggregate contact forces are in compression (shown as blue chains). Regions with a low density of force chains (shown as voids in the figure) occur directly behind the transverse ribs, indicating a local stress reduction in this location. This region can be interpreted as a zone of localized unconfined region that forms behind the transverse ribs during pullout, also referred to as the localized disturbance region (Cardile et al., 2017; Palmeira, 2004; Teixeira et al., 2007; Zhou et al., 2012). In addition, the results in Fig. 12(a) reveal a radial assembly of comparatively strong force chains in front of each transverse rib, indicating the development of localized stresses in these regions and the rotation of principal stresses during pullout. A particle-scale description of such rotation of principal stresses is the change in orientation of the contacts. Rothenburg and Bathurst (1989) proposed that the normalized contact orientation distribution $E(\theta)$ can be evaluated using a second-order Fourier series approximation (FSA) fitting, as follows:

$$E(\theta) = \frac{1}{2\pi}[1 + a_c \cos 2(\theta - \theta_c)] \tag{16}$$

where α_c is the coefficient of contact normal anisotropy and θ_c is the principal direction of the contact anisotropy. Bathurst and Rothenburg (1992) provided further mathematical interpretations of these parameters. The previous observations are consistent with the development of two shear bands, one on each side of the geogrid reinforcement. The FSA fitting results for the contacts within these two shear bands are also presented in Fig. 12(b). For the purposes of subsequent calculations, the principal direction θ_c is defined as the angle in the pullout direction. The angle in the upper shear band is defined as clockwise and that in the lower shear band as counterclockwise. The final principal directions of the contacts for the upper and lower shear bands were 56.2° and 51.1°, respectively. These values indicate the direction of the contact branch vectors and provide information about the relative positions of the particles that transfer the load. The principal directions of contact within the upper and lower shear bands are denoted as α_u and α_l, respectively, to facilitate subsequent calculations.

The rearrangement of particles caused by geogrid pullout can also be characterized by the sliding behavior of the contacts. The contacts between particles were adapted to relative sliding by adopting a limit shear force characterized by a coefficient of friction (Eq. (10). The relative sliding between particles represents the destruction and reconstruction of the local internal structure responsible for permanent specimen deformations. The fraction of sliding contacts (S_n) is defined as the ratio of the number of sliding contacts (n_s) to the total number of contacts (n_t) in a specified measurement region (V), as follows:

$$S_n = \frac{\sum_V n_s}{\sum_V n_t} \times 100\% \tag{17}$$

By dividing the entire specimen length into 30 equal-volume measurement regions along its elevation, the distribution of the fraction of sliding contacts against the distance from the geogrid location could be

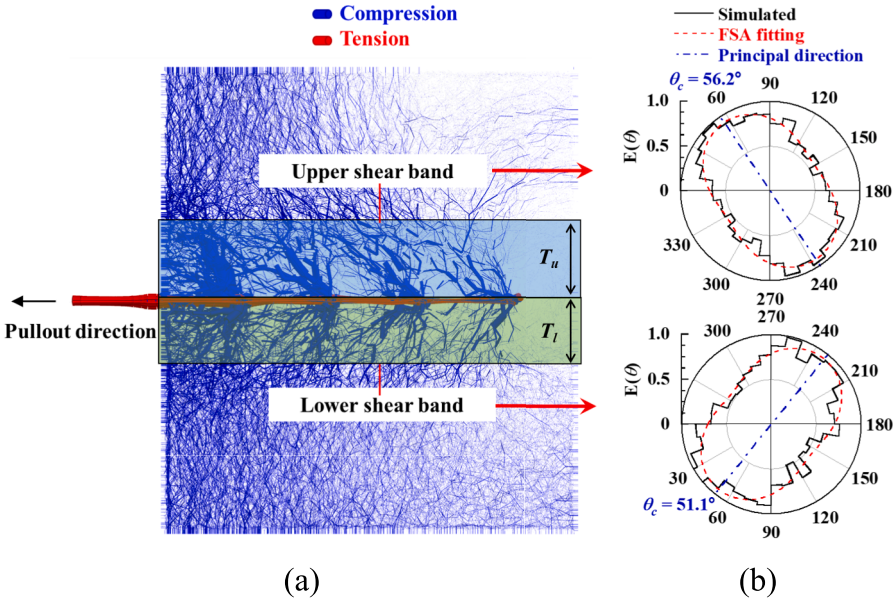

Fig. 12. Contact force chains at a pullout displacement of 48 mm: (a) visualization of force chains; and (b) distribution of contact normals in shear bands and FSA fittings.

obtained, as displayed in Fig. 13(a). As anticipated, a markedly greater fraction of sliding contacts occurred within the shear bands compared to outside the shear bands. Significant particle rearrangement occurred within this zone, resulting in a drastic evolution of the contact state. The fraction of sliding contacts towards the top of the specimen outside the shear bands was significantly higher than that near the bottom, which could be attributed to the upward climbing of particles subjected to shear under constant normal stress. The evolution of the sliding contact fraction with increasing pullout displacement is depicted in Fig. 13(b). Based on their location, contacts were categorized into three groups: aggregate-aggregate contacts within the shear bands; aggregate-aggregate contacts outside the shear bands; and geogrid-aggregate contacts (i.e., contacts immediately adjacent to the geogrid surface). The fraction of sliding contact was observed to decrease gradually, from the geogrid surface to inside the shear bands and finally outside the shear bands. On the geogrid surface, the fraction of sliding contact initially rose and then decreased slightly with larger pullout displacement. This response can be attributed to the redistribution of contact forces along the geogrid and evolution of the total geogrid-aggregate contacts. Within the shear bands, the fraction of sliding contact was found to rapidly increase before plateauing at approximately 40 %.

3.3. Geogrid deformations

The polypropylene geogrid used in this study is an extensible reinforcement material, the deformation of which can influence geogrid-aggregate interaction, which can in turn influence the mobilization of pullout resistance (Alagiyawanna et al., 2001; Cardile et al., 2017). The results shown in Fig. 14 depict the geogrid deformations at increasing pullout deflections, which are also visualized by the magnitude of the rotation of the geogrid ribs relative to their initial state. The transverse ribs possess a comparatively low bending stiffness, facilitating visualization of their deformation during pullout. Notably, the bending deformations of the transverse ribs closest to the applied frontal load were more pronounced, an effect that grew more prominent with increasing pullout displacements. The presence of highly disordered locations in the geogrid ribs were found to be caused by particles trapped within the apertures, resulting in the unevenly distributed deformations of transverse ribs to be unevenly distributed at each section. The presence of such local effects represents an additional challenge for the accurate prediction of pullout resistance via both experimental and theoretical means.

Fig. 15 displays the axial tensile strain distributions along the geogrid longitudinal ribs. The axial tensile strains are observed to decrease from a maximum value at the loaded front to zero at the embedded end. For instance, the axial tensile strains in the longitudinal ribs at Section I-I for a pullout displacement of 48 mm was 0.7 %, decreasing to 0.27 % at Section II-II. The observed non-linear decrease in axial tensile strains along the geogrid length in this study is consistent with the findings of Bathurst and Ezzein (2017), which employing a longer pullout box, demonstrated similar strain distribution behavior. In general, the axial tensile strains were observed to increase nonlinearly with increasing pullout displacement, a trend that is consistent with the results reported in experimental studies (Bathurst and Ezzein, 2017; Bergado and Chai, 1994; Morsy et al., 2019a; Palmeira, 2004; Peng and Zornberg, 2019). Furthermore, Palmeira (2004) noted that geogrid pullout results in a disturbed zone behind the transverse ribs that would affect the development of the passive resistance of adjacent transverse ribs when the spacing between transverse ribs is comparatively small. Therefore, accurate prediction of the contribution of the geogrid transverse ribs to pullout resistance requires careful evaluation of the development of axial tensile strains in the geogrid longitudinal ribs.

4. Mobilization of Pullout Resistance Components

The resistance components that develop during geogrid pullout testing can be represented by the two interaction mechanisms shown in Fig. 16 including the interface frictional resistance component (FR_{gs}) between the geogrid surface and aggregates and the passive resistance (or bearing resistance) component (PR_{gs}) generated by the transverse ribs (Cardile et al., 2017; Jewell et al., 1985; Palmeira, 2004; Sieira et al., 2009; Teixeira et al., 2007). The total pullout resistance can be calculated as $PF_t = FR_{gs} + PR_{gs}$. The evaluation of the individual resistance components based on experimental results relies on several assumptions. A common assumption is that the different pullout resistance components are activated simultaneously, with the maximum values occurring simultaneously and with these different pullout resistance components acting independently of each other. Another assumption has been that the geogrid ribs are either rigid or exhibit uniform deformation. The aforementioned assumptions rely on semi-empirical interfacial friction parameters that are back calculated from pullout test results. By removing the geogrid transverse ribs and thus any corresponding passive resistance, the frictional resistance mobilization process can be investigated separately. Fig. 17 shows a comparison of

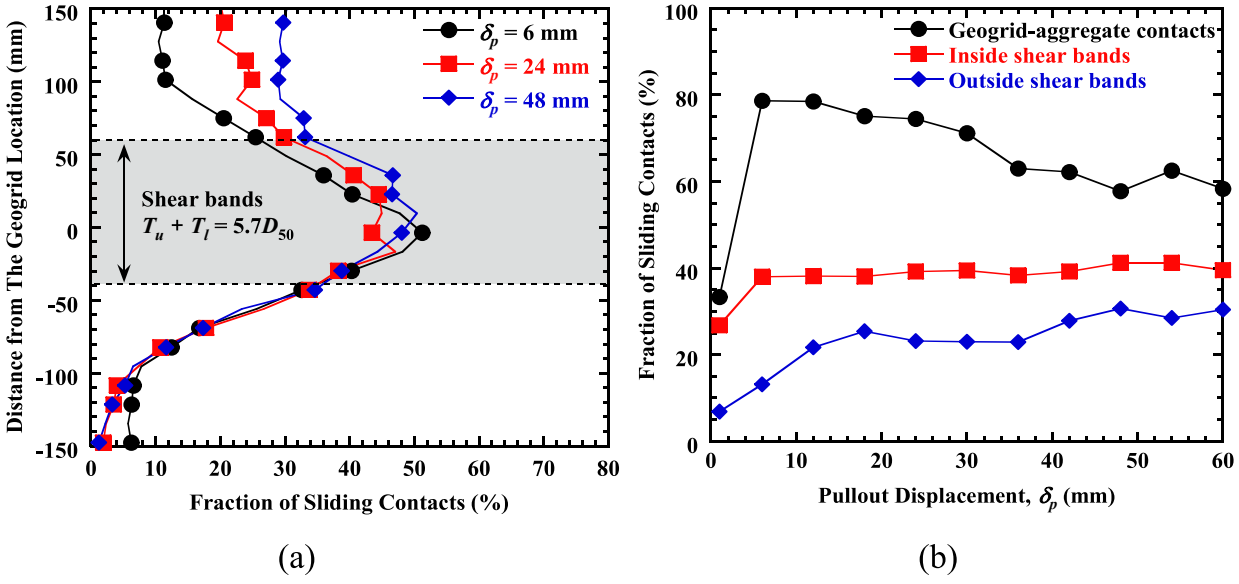

Fig. 13. Fraction of sliding contacts: (a) distribution; and (b) evolution.

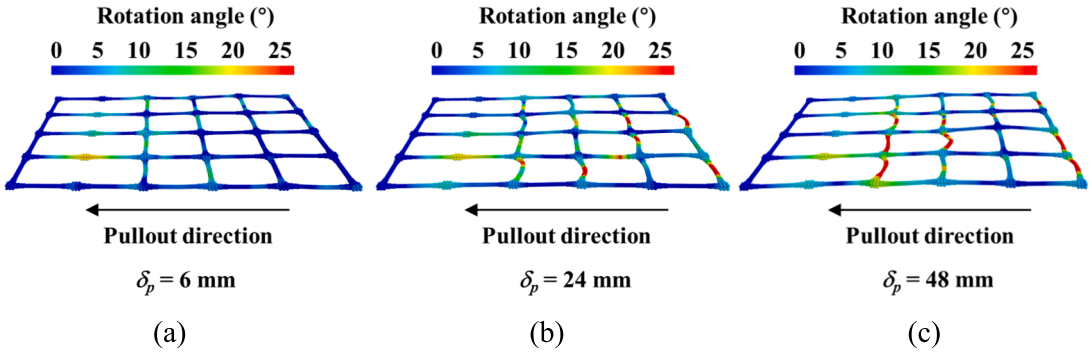

Fig. 14. Geogrid deformations at different pullout displacements: (a) δ_p = 6 mm; (b) δ_p = 24 mm; and (c) δ_p = 48 mm.

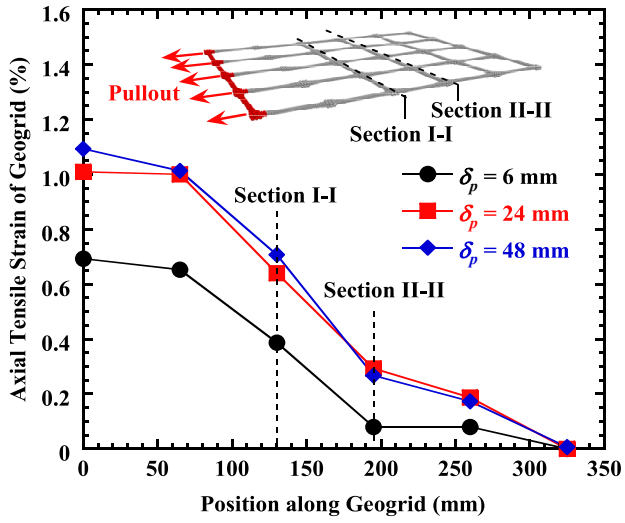

Fig. 15. Axial tensile strain distributions along longitudinal ribs.

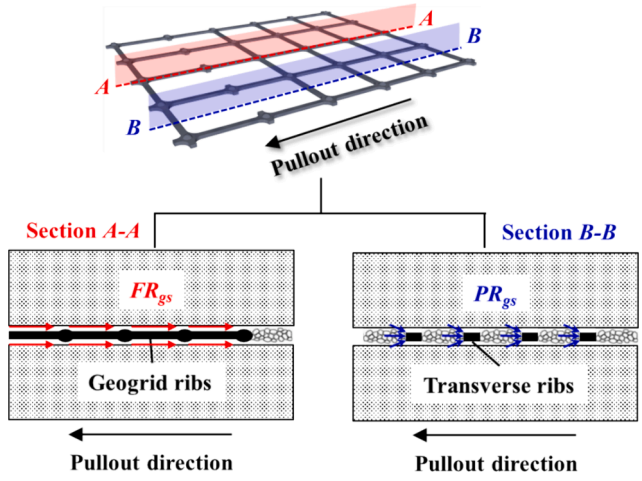

Fig. 16. Pullout resistance components.

simulated pullout test results involving geogrids with and without transverse ribs under a normal stress σ_n = 12.5 kPa. The shear displacement corresponding to the ultimate pullout resistance is reasonably different for these two cases. This suggests that the passive resistance and frictional resistance components may not have been activated simultaneously for the extensible reinforcement. Accurately predicting individual pullout resistance components is challenging

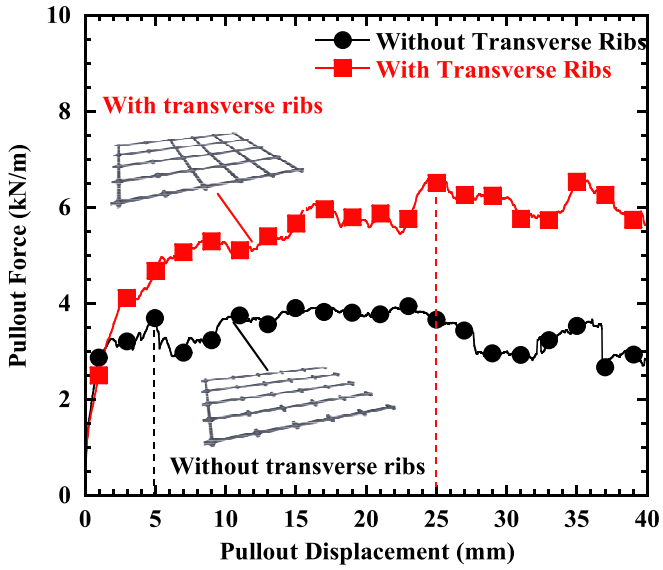

Fig. 17. Comparison of pullout test predictions involving geogrids with and without transverse ribs.

because of the randomness of the particle arrangement, localized stress concentration and transfer, and complex interlocking mechanisms.

This study proposes an approach to evaluate and track the mobilization of the pullout resistance components based on contact identification using the DEM simulation results. An essential step in this approach involves identifying the contacts that contribute to the passive resistance of the transverse ribs (PR_{gs}) based on DEM simulation results. The contact types associated with the aggregate-transverse ribs were initially identified, as illustrated in Fig. 18(a) for one of the transverse geogrids. Next, the angle between the branch vector direction of these contacts and the projection of the pullout direction in the x-o-z plane was determined to assess whether it was smaller than the principal direction (angle in the pullout direction) of the contact normal within the shear band (Fig. 18b). In this case, these contacts were identified as contributing to the passive resistance of the transverse ribs, and the contact force component in the pullout direction, f_x, was quantified. Finally, the overall passive resistance component could be calculated from the contribution of the individual transverse as $PR_{gs} = \sum f_x$. The frictional component was obtained by subtracting the magnitude of the passive resistance component from the amplitude of the total pullout force ($FR_{gs} = PF_t - PR_{gs}$).

Fig. 19 shows the mobilization of the total pullout force and individual pullout resistance components with increasing pullout displacements. At the initial stages of pullout testing, the frictional resistance component was mobilized first and quickly reached its peak value. On

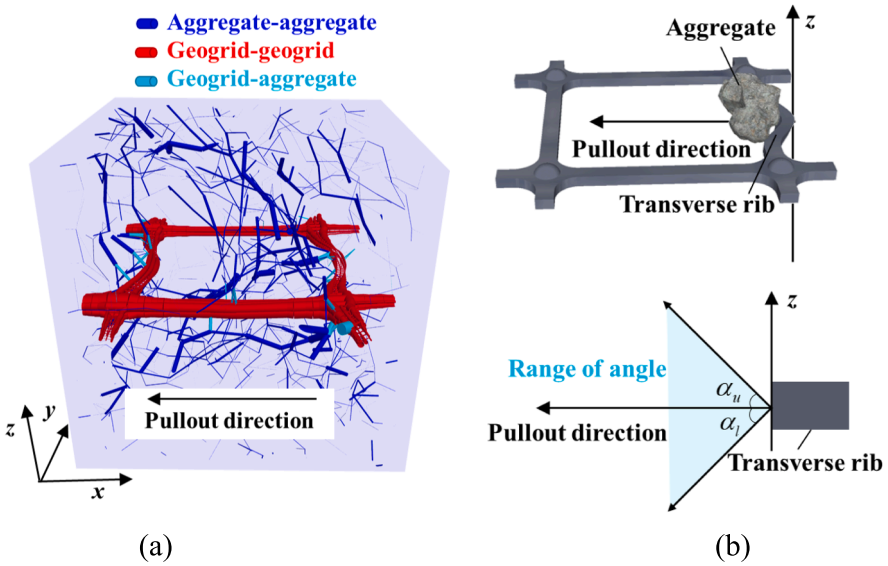

Fig. 18. Identification of contacts contributing to the passive resistance of transverse ribs: (a) contact force distribution mobilized in an aperture; and (b) angle between the branch vector of aggregate-transverse rib contacts and the pullout direction.

the other hand, the passive resistance component of the transverse ribs increased gradually and only reached a peak value after a comparatively large pullout displacement had occurred. These results indicate that the individual resistance components are not simultaneously mobilized during pullout. This observation indicates that the contact between the geogrid and cohesionless aggregates allows the activation of frictional resistance after very small displacements. In contrast, the mobilization of the transverse rib passive resistance requires larger relative displacements to accommodate the deformations. This observation also corroborates the findings of Bathurst and Ezzein (2017) regarding the significant contribution of aggregate soil trapped between transverse members to the overall pullout resistance of geogrids.

As geogrid pullout continued, the frictional resistance component was observed to fluctuate after reaching its peak, but showed an overall decreasing trend. Instead, the passive resistance component of the transverse ribs was also observed to fluctuate, but it maintained a reasonably constant value after reaching its peak. These observations indicate that the internal structure of the specimen underwent cycles of destruction and reconstruction. A comparison of the results for different normal stresses revealed that the peak value of the passive resistance component of the transverse ribs in all cases was reached after the ultimate pullout resistance had been reached. Results also indicate that the peak frictional resistance component value increased significantly with increasing normal stresses, and the activation of the transverse rib passive resistance required comparatively large pullout displacements.

5. Influence of geogrid stiffness

The tensile stiffness of geogrids has been reported to affect pullout behavior significantly (Bergado and Chai, 1994). The tensile stiffness values of several typical geogrids used in field projects range from 330 kN/m to 1185 kN/m (Jia et al., 2021; Jiang et al., 2016; Yang et al., 2012). To investigate the influence of geogrid stiffness (e.g., secant stiffness at 2 % strain $J_{2\%}$) on the passive resistance of transverse ribs, several additional numerical simulations were conducted using geogrids with secant stiffnesses in the MD direction of $J_{2\%} = 325$ kN/m, 650 kN/m, and 1300 kN/m. A consistent stiffness ratio ($J^{MD}_{2\%}/J^{CMD}_{2\%}$) of 1.15 was maintained between the transverse and longitudinal ribs for the different geogrid models. A normal stress $\sigma_n = 12.5$ kPa was adopted in the numerical simulations.

Fig. 20 presents the mobilization of pullout resistance components for specimens with different geogrid stiffness values. As illustrated in Fig. 20(a), the transverse rib passive resistance was found to increase significantly with increasing geogrid stiffness. That is, a relatively high geogrid stiffness facilitates the rapid mobilization of the transverse rib passive resistance. A higher tensile stiffness enhances the geogrid flexural stiffness, allowing the transverse ribs to provide passive resistance with smaller deformations. Moreover, higher geogrid stiffness leads to higher peak passive resistance of the transverse ribs, confirming that higher geogrid stiffness promotes an ongoing increase in the transverse rib passive resistance. However, after the peak value was reached, the frictional resistance components of each specimen showed a fluctuating decreasing trend that reduced slightly with increasing geogrid stiffness. Overall, the frictional resistance of the geogrid was found not to be significantly affected by geogrid stiffness.

6. Conclusions

In this study, three-dimensional (3D) Discrete Element Method (DEM) analyses simulating pullout tests of geogrids embedded in clean aggregates were conducted to investigate the interaction mechanisms that develop during load mobilization. The DEM models were initially calibrated using the experimental results from pullout tests. The DEM simulations allowed obtaining the distribution of particle displacement fields, the shear bands, the distribution of contact forces within these shear bands, and the deformation patterns of the geogrids. Interpretation of the DEM simulation results facilitated understanding the mobilization of the different pullout resistance components as well as the influence of the geogrid stiffness on these components. The following conclusions were drawn:

(1) Shear bands were found to initiate from the geogrid surface, becoming increasingly thicker with increasing pullout displacements. Significant geogrid-aggregate interaction occurred within the shear bands, which were uniformly distributed along the plane of the geogrid in the pullout direction. The shear bands that developed on either side of the geogrid were found not to be symmetrical, with the upper shear band being slightly thicker than the lower one due to the more compliant horizontal loading arrangement.

(2) Significant particle rearrangement was found to occur within the shear bands, resulting in a sharp mobilization of the contact state. The fraction of sliding contacts that developed towards the top of the specimen (beyond the shear bands) was considerably higher than toward the

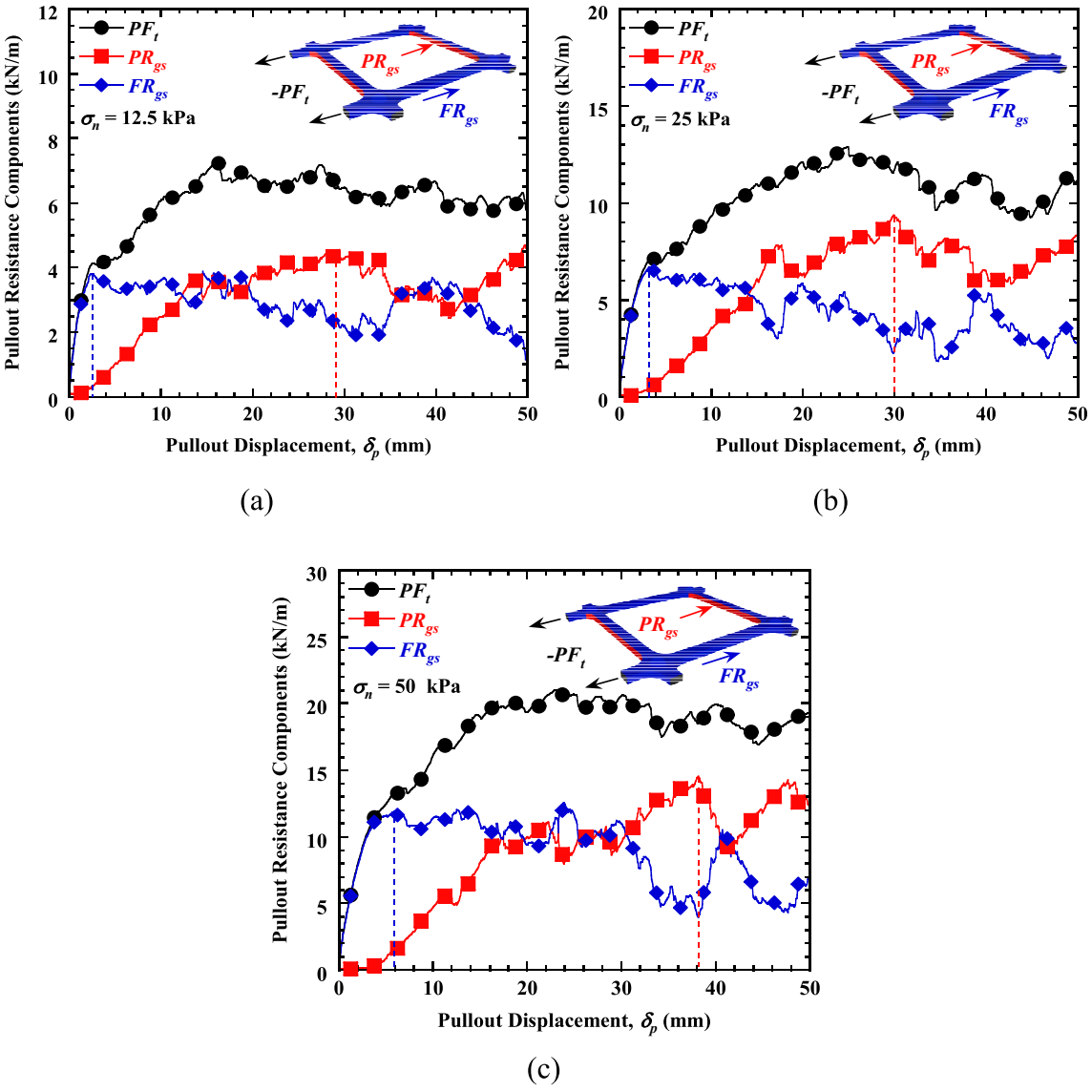

Fig. 19. Pullout force and pullout resistance component mobilization: (a) σ_n = 12.5 kPa; (b) σ_n = 25 kPa; and (c) σ_n = 50 kPa.

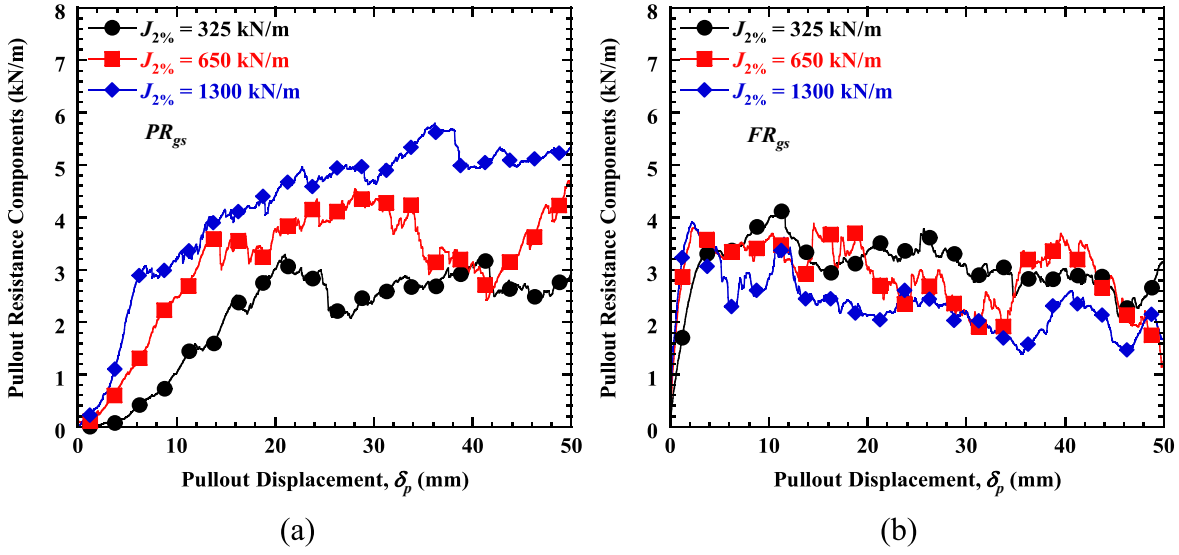

Fig. 20. Mobilization of pullout resistance components for different geogrid stiffness values: (a) PR_{gs}; and (b) FR_{gs}.

bottom, which can be attributed to the upward climbing of particles (i.e., dilation) that developed during shearing under constant normal stress and was permitted by the more compliant horizontal loading arrangement.

(3) Bending deformations of the transverse ribs located close to the frontal loading were found to be comparatively more prominent, especially as pullout displacement increased. Also, the deformation distribution along a given transverse rib was not uniform, as it depended on the local presence of individual particles causing interlocking with the geogrid. Specifically, in locations along the transverse rib where interlocking is more significant, the deformation of the transverse rib was found to be comparatively greater, leading to a more significant mobilization of passive resistance. The changes in geogrid strains (i.e. its curvature) were found to decrease from the frontal loading to the embedment end. Also, the geogrid axial tensile strains were observed to increase nonlinearly with increasing pullout displacements.

(4) The individual resistance components were found not to mobilize simultaneously during geogrid pullout. While the frictional resistance component was mobilized under very small displacements, the passive resistance mobilized by the transverse ribs required comparatively large displacements. As normal stress increased, the peak values of both the frictional resistance component and the passive resistance component increased, and mobilization of the passive resistance required a greater pullout displacement.

(5) The stiffness of the geogrids was found to significantly impact the passive resistance provided by transverse ribs, with increasing stiffness resulting in significant increases in passive resistance. High geogrid stiffness was also found to contribute to a rapid mobilization of passive resistance by the transverse ribs. That is, a comparatively high geogrid tensile stiffness contributed to an increasing bending stiffness, which in turn allowed transverse ribs to offer passive resistance at comparatively small displacements. The frictional resistance component, however, was found to be comparatively insensitive to the geogrid stiffness.

CRediT authorship contribution statement

Yafei Jia: Writing – original draft, Methodology, Investigation, Formal analysis, Data curation. **Jorge G. Zornberg:** Writing – review & editing, Resources. **Jun Zhang:** Resources, Project administration, Funding acquisition. **Jun-Jie Zheng:** Supervision, Project administration, Funding acquisition. **Yewei Zheng:** Writing – review & editing, Supervision, Project administration, Funding acquisition, Conceptualization.

Declaration of competing interest

The authors declare that they have no known competing financial interests or personal relationships that could have appeared to influence the work reported in this paper.

Data availability

Data will be made available on request.

Acknowledgments

This research is supported by the National Natural Science Foundation of China (Grant No. 52278360 and 52078392), the Fundamental Research Funds for the Central Universities (Grant No. 2042023kfyq03 and 2042023kf1014), and the National Key R&D Program of China (Grant No. 2022YFC3080400). The authors gratefully acknowledge the financial supports. The first author appreciates the financial support from the Special Scholarship for Graduate Students' International Exchange Program of Wuhan University.

References

Abdi, M.R., Arjomand, M.A., 2011. Pullout tests conducted on clay reinforced with geogrid encapsulated in thin layers of sand. Geotext. Geomembr. 29, 588–595.
Abdi, M.R., Mirzaeifar, H., 2017. Experimental and PIV evaluation of grain size and distribution on soil-geogrid interactions in pullout test. Soils Found. 57, 1045–1058.
Alagiyawanna, A.M.N., Sugimoto, M., Sato, S., Toyota, H., 2001. Influence of longitudinal and transverse members on geogrid pullout behavior during deformation. Geotext. Geomembr. 19, 483–507.
ASTM, 2015. Standard test method for determining tensile properties of geogrids by the single or multi-rib tensile method. ASTM D6637. West Conshohocken, PA: ASTM.
Bathurst, R.J., Ezzein, F.M., 2015. Geogrid and soil displacement observations during pullout using a transparent granular soil. Geotech. Test. J. 38, 673–685.
Bathurst, R.J., Ezzein, F.M., 2017. Insights into geogrid–soil interaction using a transparent granular soil. Géotech. Lett. 7, 179–183.
Bathurst, R.J., Naftchali, F.M., 2021. Geosynthetic reinforcement stiffness for analytical and numerical modelling of reinforced soil structures. Geotext. Geomembr. 49, 921–940.
Bathurst, R.J., Rothenburg, L., 1992. Investigation of micromechanical features of idealized granular assemblies using DEM. Eng. Comput. 9, 199–210.
Bergado, D.T., Chai, J.C., 1994. Pullout force/displacement relationship of extensible grid reinforcements. Geotext. Geomembr. 13, 295–316.
Cardile, G., Gioffre, D., Moraci, N., Calvarano, L.S., 2017. Modelling interference between the geogrid bearing members under pullout loading conditions. Geotext. Geomembr. 45, 169–177.
Chen, C., McDowell, G., Rui, R., 2018. Discrete element modelling of geogrids with square and triangular apertures. Geomech. Eng. 16, 495–501.
Cundall, P.A., Strack, O.D.L., 1979. A discrete numerical model for granular assemblies. Geotechnique 29, 47–65.
DeJong, J.T., Westgate, Z.J., 2009. Role of initial state, material properties, and confinement condition on local and global soil-structure interface behavior. J. Geotech. Geoenviron. Eng. 135, 1646–1660.
Derksen, J., Ziegler, M., Fuentes, R., 2021. Geogrid-soil interaction: a new conceptual model and testing apparatus. Geotext. Geomembr. 49, 1393–1406.
Druckrey, A.M., Alshibli, K.A., 2017. 3D Particle-Scale Displacement Gradient to Uncover the Onset of Shear Bands in Sand, Bifurcation and Degradation of Geomaterials with Engineering Applications, pp. 39-45.
Ezzein, F.M., Bathurst, R.J., 2014. A new approach to evaluate soil-geosynthetic interaction using a novel pullout test apparatus and transparent granular soil. Geotext. Geomembr. 42, 246–255.
Feng, S.J., Wang, Y.Q., 2023. DEM simulation of geogrid-aggregate interface shear behavior: Optimization of the aperture ratio considering the initial interlocking states. Comput. Geotech. 154.
Ferellec, J.-F., McDowell, G.R., 2010. A method to model realistic particle shape and inertia in DEM. Granul. Matter 12, 459–467.
Ferellec, J.F., McDowell, G.R., 2012. Modelling of ballast-geogrid interaction using the discrete-element method. Geosynth. Int. 19, 470–479.
Ferreira, F.B., Vieira, C.S., Lopes, M.L., Carlos, D.M., 2015. Experimental investigation on the pullout behaviour of geosynthetics embedded in a granite residual soil. Eur. J. Environ. Civ. Eng. 20, 1147–1180.
Gao, G., Meguid, M.A., 2018. Effect of particle shape on the response of geogrid-reinforced systems: Insights from 3D discrete element analysis. Geotext. Geomembr. 46, 685–698.
Grabowski, A., Nitka, M., Tejchman, J., 2021. Comparative 3D DEM simulations of sand-structure interfaces with similarly shaped clumps versus spheres with contact moments. Acta Geotech. 16, 3533–3554.
Gu, M., Han, J., Zhao, M., 2017. Three-dimensional DEM analysis of single geogrid-encased stone columns under unconfined compression: a parametric study. Acta Geotech. 12, 559–572.
Han, J., Bhandari, A., Wang, F., 2012. DEM analysis of stresses and deformations of geogrid-reinforced embankments over piles. Int. J. Geomech. 12, 340–350.
Hussein, M.G., Meguid, M.A., 2016. A three-dimensional finite element approach for modeling biaxial geogrid with application to geogrid-reinforced soils. Geotext. Geomembr. 44, 295–307.
Hussein, M.G., Meguid, M.A., 2020. Improved understanding of geogrid response to pullout loading: insights from three-dimensional finite-element analysis. Can. Geotech. J. 57, 277–293.
Indraratna, B., Ngo, N.T., Rujikiatkamjorn, C., 2013. Deformation of coal fouled ballast stabilized with geogrid under cyclic load. J. Geotech. Geoenviron. Eng. 139, 1275–1289.
Jewell, R.A., Milligan, G.W.E., Sarsby, R.W., Dubois, D., 1985. Interaction between Soil and Geogrids. Proc., Conference on Polymer Grid Reinforcement, London, pp.18-29.
Jia, Y., Zhang, J., Chen, X., Miao, C., Zheng, Y., 2023. DEM study on shear behavior of geogrid-soil interfaces subjected to shear in different directions. Comput. Geotech. 156.
Jia, Y., Zhang, J., Ngo, T., Zheng, Y., 2024. Shear resistance evolution of geogrid-aggregate interfaces under direct shear: insights from 3D DEM simulations. Can. Geotech. J.
Jia, M., Zhu, W., Xu, C., 2021. Performance of a 33m high geogrid reinforced soil embankment without concrete panel. Geotext. Geomembr. 49, 122–129.
Jiang, Y., Han, J., Parsons, R.L., Brennan, J.J., 2016. Field instrumentation and evaluation of modular-block mse walls with secondary geogrid layers. J. Geotech. Geoenviron. Eng. 142.
Jing, X.-Y., Zhou, W.-H., Zhu, H.-X., Yin, Z.-Y., Li, Y., 2018. Analysis of soil-structural interface behavior using three-dimensional DEM simulations. Int. J. Numer. Anal. Meth. Geomech. 42, 339–357.

Lashkari, A., Jamali, V., 2021. Global and local sand–geosynthetic interface behaviour. Géotechnique 71, 346–367.
Leshchinsky, D., Imamoglu, B., Meehan, C.L., 2010. Exhumed geogrid-reinforced retaining wall. J. Geotech. Geoenviron. Eng. 136, 1311–1323.
Liu, C.-N., Ho, Y.-H., Huang, J.-W., 2009a. Large scale direct shear tests of soil/PET-yarn geogrid interfaces. Geotext. Geomembr. 27, 19–30.
Liu, H.L., Ng, C.W.W., Fei, K., 2007. Performance of a geogrid-reinforced and pile-supported highway embankment over soft clay: case study. J. Geotech. Geoenviron. Eng. 133, 1483–1493.
Liu, F.Y., Ying, M.J., Yuan, G.H., Wang, J., Gao, Z.Y., Ni, J.F., 2021. Particle shape effects on the cyclic shear behaviour of the soil-geogrid interface. Geotext. Geomembr. 49, 991–1003.
Liu, C.N., Zornberg, J.G., Chen, T.C., Ho, Y.H., Lin, B.H., 2009b. Behavior of geogrid-sand interface in direct shear mode. J. Geotech. Geoenviron. Eng. 135, 1863–1871.
Mahigir, A., Ardakani, A., Hassanlourad, M., 2021. Comparison between monotonic, cyclic and post-cyclic pullout behavior of a pet geogrid embedded in clean sand and clayey sand. Int. J. Geosynth. Ground Eng. 7.
Miao, C.X., Jia, Y.F., Zhang, J., Zhao, J.B., 2020. DEM simulation of the pullout behavior of geogrid-stabilized ballast with the optimization of the coordination between aperture size and particle diameter. Constr. Build. Mater. 255.
Miao, C., Zheng, J., Zhang, R., Cui, L., 2017. DEM modeling of pullout behavior of geogrid reinforced ballast: the effect of particle shape. Comput. Geotech. 81, 249–261.
Moraci, N., Recalcati, P., 2006. Factors affecting the pullout behaviour of extruded geogrids embedded in a compacted granular soil. Geotext. Geomembr. 24, 220–242.
Morsy, A.M., Zornberg, J.G., Han, J., Leshchinsky, D., 2019a. A new generation of soil-geosynthetic interaction experimentation. Geotext. Geomembr. 47, 459–476.
Morsy, A.M., Zornberg, J.G., Leshchinsky, D., Han, J., 2019b. Soil-Reinforcement Interaction: effect of reinforcement spacing and normal stress. J. Geotech. Geoenviron. Eng. 145.
Ngo, N.T., Indraratna, B., Rujikiatkamjorn, C., 2014. DEM simulation of the behaviour of geogrid stabilised ballast fouled with coal. Comput. Geotech. 55, 224–231.
Palmeira, E.M., 2004. Bearing force mobilisation in pull-out tests on geogrids. Geotext. Geomembr. 22, 481–509.
Palmeira, E.M., 2009. Soil–geosynthetic interaction: modelling and analysis. Geotext. Geomembr. 27, 368–390.
Palmeira, E.M., Milligan, G.W.E., 1989. Scale and other factors affecting the results of pull-out tests of grids buried in sand. Géotechnique 39, 511–524.
Peng, X., Zornberg, J.G., 2019. Evaluation of soil-geogrid interaction using transparent soil with laser illumination. Geosynth. Int. 26, 206–221.
Potyondy, D.O., Cundall, P.A., 2004. A bonded-particle model for rock. Int. J. Rock Mech. Min. Sci. 41, 1329–1364.
Roodi, G.H., Zornberg, J.G., 2017. Stiffness of soil-geosynthetic composite under small displacements. ii: experimental evaluation. J. Geotech. Geoenviron. Eng. 143.
Rothenburg, L., Bathurst, R.J., 1989. Analytical study of induced anisotropy in idealized granular materials. Geotechnique 39, 601–614.
Rowe, R.K., Li, A.L., 2005. Geosynthetic-reinforced embankments over soft foundations. Geosynth. Int. 12, 50–85.
Shinoda, M., Bathurst, R., 2004. Strain measurement of geogrids using a video-extensometer technique. Geotech. Test. J. 27, 456–463.
Sieira, A.C.C.F., Gerscovich, D.M.S., Sayão, A.S.F.J., 2009. Displacement and load transfer mechanisms of geogrids under pullout condition. Geotext. Geomembr. 27, 241–253.
Stahl, M., Konietzky, H., te Kamp, L., Jas, H., 2014. Discrete element simulation of geogrid-stabilised soil. Acta Geotech. 9, 1073–1084.
Sugimoto, M., Alagiyawanna, A.M.N., 2003. Pullout behavior of geogrid by test and numerical analysis. J. Geotech. Geoenviron. Eng. 129, 361–371.
Sugimoto, M., Alagiyawanna, A.M.N., Kadoguchi, K., 2001. Influence of rigid and flexible face on geogrid pullout tests. Geotext. Geomembr. 19, 257–277.
Teixeira, S.H.C., Bueno, B.S., Zornberg, J.G., 2007. Pullout resistance of individual longitudinal and transverse geogrid ribs. J. Geotech. Geoenviron. Eng. 133, 37–50.
Tutumluer, E., Huang, H., Bian, X.C., 2012. Geogrid-aggregate interlock mechanism investigated through aggregate imaging-based discrete element modeling approach. Int. J. Geomech. 12, 391–398.
Vangla, P., Latha, G.M., 2015. Influence of particle size on the friction and interfacial shear strength of sands of similar morphology. Int. J. Geosynth. Ground Eng. 1, 6.
Wang, Y., Cui, X., Liu, K., Jiang, P., 2022. Manufacture, development, and application of sensor-enabled geosynthetics: state-of-the-art review. Intelligent Transportation Infrastructure 1, liac012.
Wang, Y., Feng, S., 2023. Discrete element analysis of geogrid–aggregate interface shear behavior under cyclic normal loading. Can. Geotech. J.
Wang, Y.-Q., Feng, S.-J., Zhao, Y., Zheng, Q.-T., 2024. Microscale analysis of geogrid–aggregate interface cyclic shear behavior using DEM. Comput. Geotech. 166, 105973.
Wang, Z.J., Jacobs, F., Ziegler, M., 2014. Visualization of load transfer behaviour between geogrid and sand using PFC2D. Geotext. Geomembr. 42, 83–90.
Wang, Z., Xia, Q., Yang, G., Zhang, W., Zhang, G., 2023. Effects of transverse members on geogrid pullout behavior considering rigid and flexible top boundaries. Geotext. Geomembr. 51, 72–84.
Yang, G., Liu, H., Lv, P., Zhang, B., 2012. Geogrid-reinforced lime-treated cohesive soil retaining wall: case study and implications. Geotext. Geomembr. 35, 112–118.
Zhou, J., Chen, J.F., Xue, J.F., Wang, J.Q., 2012. Micro-mechanism of the interaction between sand and geogrid transverse ribs. Geosynth. Int. 19, 426–437.
Zornberg, J.G., Sitar, N., Mitchell, J.K., 2000. Performance of geosynthetic reinforced slopes at failure. J. Geot. Geoenviron. Eng. 124, 670–683.